Computation of permeability of a non-crimp carbon textile reinforcement based on X-ray computed tomography images

Ilya Straumit[a*], Christoph Hahn[c], Elisabeth Winterstein[c], Bernhard Plank[b], Stepan V. Lomov[a], Martine Wevers[a]

[a]*Department of Materials Engineering, KU Leuven, Belgium*
[b]*Fakultaet für Technik und Umweltwissenschaften, University of Applied Sciences Upper Austria, Austria*
[c]*Lehrstuhl für Carbon Composites, Technische Universitaet Muenchen (TUM), Germany*
*straumit.ilya@mtm.kuleuven.be; phone: +3216373488

Abstract

The paper demonstrates the possibility of a correct (within the experimental scatter) calculation of a textile reinforcement permeability based on X-ray micro-computed tomography registration of the textile internal architecture, introduces the image segmentation procedures to achieve the necessary precision of reconstruction of the geometry and studies variability of the geometry and local permeability. The homogenized permeability of a non-crimp textile reinforcement is computed using computational fluid dynamics with voxel geometrical models. The models are constructed from X-ray computed tomography images using a statistical image segmentation method based on a Gaussian mixture model. The computed permeability shows a significant variability across different unit cells, in the range of $(0.5\ldots3.5)\times10^{-4}$ mm^2, which is strongly correlated with the solid volume fraction in the unit cell.

Keywords: A. Carbon fibre; A. Fabrics/textiles; C. Computational modelling; D. Non-destructive testing.

1. Introduction

Fabrication of fibre reinforced composites by (liquid) composite moulding involves impregnation of the dry reinforcement with a low viscosity resin, which is injected into the mould cavity [1]. In the process of impregnation, the liquid resin flows through the system of channels inside the reinforcement, which can be considered as a porous medium. The flow of a liquid through a porous medium is described by the Darcy's law, which states a dependence of the flow velocity on the permeability of the medium, viscosity of the liquid and the applied pressure gradient. The permeability of the composite reinforcement is determined by the size and shape of the flow channels inside it; it is usually anisotropic and can be described by a second order tensor. Permeability is an important parameter of the technological process, which determines the quality of the impregnation and the duration of

the production cycle. For the simplest and ideal case of unidirectional arrangement of fibres, analytical models have been developed, which allow to calculate the longitudinal and transversal permeability as a function of the fibre radius and volume fraction [2, 3]. The structure of textile fabrics is more complex and includes two levels – the channel network between the yarns, and the intra-yarn channels, where the liquid can flow in the space between fibres [4]. The intra-yarn structure can be considered as a unidirectional arrangement of fibres; its permeability can be estimated from analytical models with fair accuracy. The level of yarns, however, is more complex; its contribution to the permeability of the preform is determined by the parameters of the preform: weave type, fibre volume fraction, yarn linear density, sett and crimp [5, 6]. Calculation of the permeability of composite preforms can be done by numerical methods, through the flow simulations, but it requires a detailed description of the geometry of the flow channels.

A number of architecture-specific approaches to the estimation of permeability of composite preforms were developed, which use idealized models of the flow channels in the preform [7-12]. Calculation of the permeability on the basis of a constructed model can be done through the solution of the Navier-Stokes or Stokes equations with finite element [13] or finite difference [14] discretization. More realistic models can take into account perturbations of the geometry or the features introduced in manufacturing of the fabric [15-18]. Stochastic models of the reinforcement, calibrated using X-ray computed tomography (μCT) data, allow generating virtual instances of the material [19-21]. Application of μCT to the permeability determination involves processing of three-dimensional images of composite samples to extract geometrical characteristics of the preform and use these data to construct a model directly or to combine them with an ideal model. As the permeability of a preform depends on the geometry and the volumetric fraction of flow channels, the most important step in the modelling is the image segmentation, which extracts the phase boundaries. Usually this is done using grey-value thresholding [22, 23], however this method requires re-calibration of the algorithm with experimental data for each image due to the fact the threshold is specific for the image acquisition parameters and the type of material. Up to now the image segmentation methods were not precise enough to allow calculation of the textile permeability (which is extremely sensitive to the details of geometrical reconstruction) with the precision with experimental scatter. At least (to the best knowledge of the authors) there is no published demonstration of such calculation. In the present paper we demonstrate that this goal can be achieved.

This paper presents the results on the determination of the permeability of a non-crimp carbon textile reinforcement based on μCT images. The computation of the permeability is done using simulations of the fluid dynamics with voxel models, constructed from the μCT images of the material samples. The voxel models are constructed using a statistical algorithm for image segmentation, based on the Gaussian mixture model, which belongs to

the class of supervised classification. This method does not require calibration with experimental data due to the fact that it is based on the quantities, extracted from a μCT image, which reflect local physical properties of the material. The results are validated with experimental data. The validated calculation of permeability allows studying its variability for different unit cells of the textile, extracted from an image of the same sample.

The paper is structured as follows. Section 2 describes the material, the samples and the μCT used in the study. Section 3 describes the segmentation algorithm. Section 4 explains the computation procedure for the permeability. Section 5 presents the results, including comparison with experiment and variability study, and section 6 contains the discussion and conclusions.

2. Material, samples and micro-CT imaging

The material used in the study is a non-crimp carbon/epoxy composite from Saertex (540 g/m^2, +45/-45, franse stitch). The manufactured test plate had a thickness of 4.0 mm and a resulting fibre volume fraction of 45.5%. The plate was produced from six layers of the dry fabric impregnated by the resin RIM 135 and the hardener RIMH 136.6 from Momentive, and cured at a temperature of 25°C. The data on the permeability of the studied NCF reinforcement is presented in [24]: at a fibre volume fraction of 50.8% the saturated permeability was measured as 0.5×10^{-4} mm^2 (in the 45° direction to the production direction). Based on linear fit of the fibre volume fraction – log (permeability) dependencies presented in [25] for non-crimp fabrics, similar to the one studied here, the permeability at fibre volume fraction of 45.5% can be estimated as $(1\ldots2)\times10^{-4}$ mm^2. Three samples of different size were cut from the plate and scanned with the Nanotom X-ray computed tomography system (General Electrics). The dimensions of the samples, the resolution of the image and the number of unit cells (representative volume elements) in each sample are given in Table 1. The size of the unit cell was obtained by measuring bundle insertion density with ImageJ. Cross-sections of the micro-CT images are shown in Fig. 1.

Table 1. Dimensions of the samples, image resolution and number of unit cells.

	Dimensions, mm	**Resolution of micro-CT image, μm**	**Number of unit cells**
Sample #1	2.45 × 3.78 × 4.00	2.25	1×2
Sample #2	9.79 × 8.32 × 4.00	6.00	4×4
Sample #3	6.32 × 5.93 × 4.00	4.20	3×3

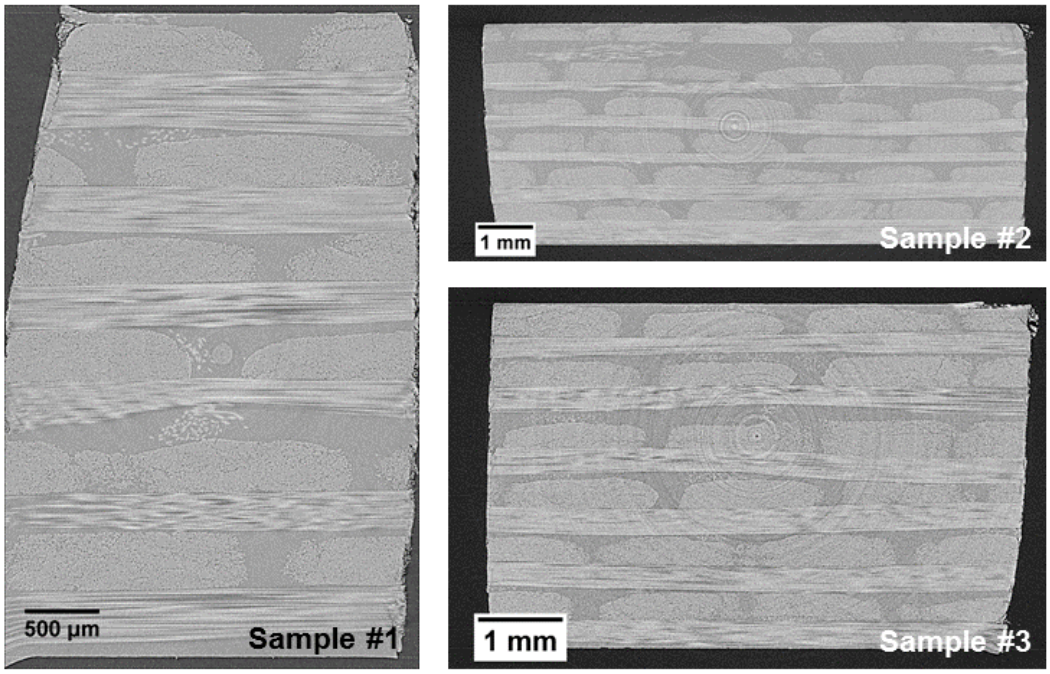

Fig. 1. Micro-CT images of the carbon/epoxy samples, cross-sections orthogonal to the sample rotation axis in the micro-CT scanner. The ring-like structures visible in the images are ring artefacts, which are common in micro-CT imaging.

3. Image segmentation algorithm

In the context of the present study, segmentation is a problem of finding in the image a set of non-overlapping domains, corresponding to the components of the voxel[1] model, which are solid and fluid phases. The task of segmentation therefore involves classification of each voxel of the model into a finite set of classes. This classification was done using two feature variables: average grey value and structural anisotropy. Denoting the grey value distribution in the image as $I(\boldsymbol{p})$, the average grey value is calculated as:

$$g(\boldsymbol{p}) = \int_W I(\boldsymbol{p} + \boldsymbol{r}) d\boldsymbol{r}$$

where W is the integration window, and $d\boldsymbol{r} = dx_1 dx_2 dx_3$. Structural anisotropy is defined as follows:

$$\beta(\boldsymbol{p}) = 1 - \frac{\lambda_1}{\lambda_3}$$

where $\lambda_1 \leq \lambda_2 \leq \lambda_3$ are the eigenvalues of structure tensor:

[1]The term "voxel" in this context refers to an element of a model rather than to a pixel of a 3D image.

$$S_{ij}(\boldsymbol{p}) = \int_W \frac{\partial I(\boldsymbol{p}+\boldsymbol{r})}{\partial x_i} \frac{\partial I(\boldsymbol{p}+\boldsymbol{r})}{\partial x_j} d\boldsymbol{r}$$

Here vector **p** defines the position of the centre of the integration window in the global coordinate system of the image. Vector **r** is the relative position of a pixel of the image inside the integration window (Fig 2).

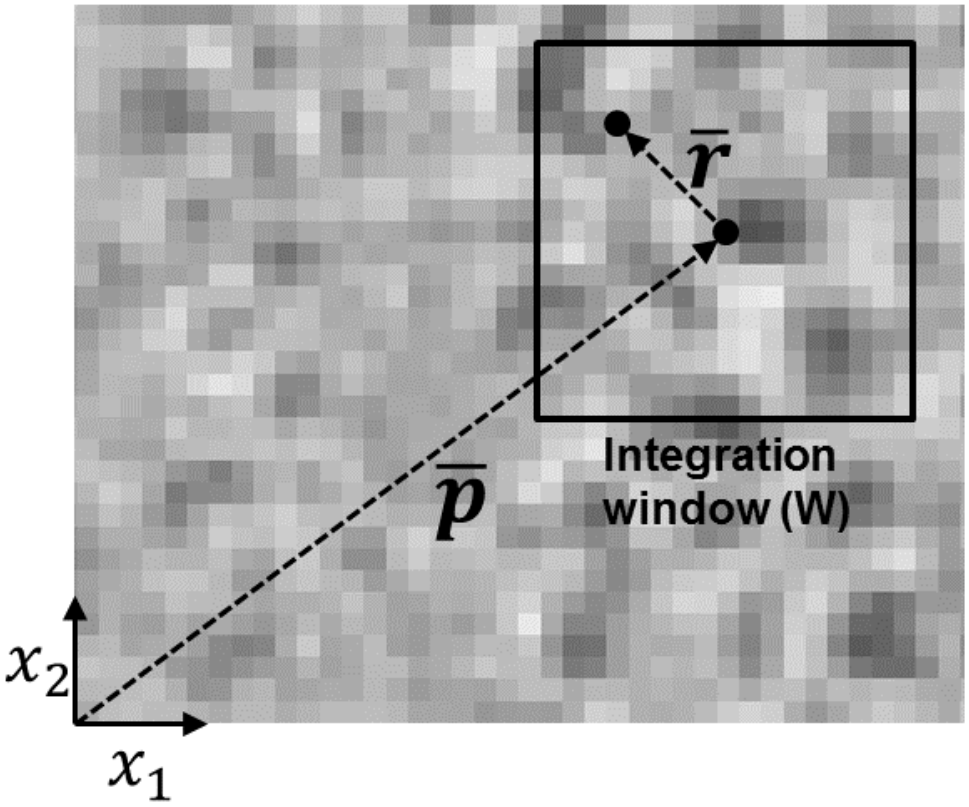

Fig. 2. A magnified micro-CT image, illustrating the relation between the integration window and the vectors **p** and **r** used in calculation of the average grey value and structural anisotropy. Vector **p** defines the centre of the current integration window; vector **r** defines the position of a pixel of the image inside the integration window. Actual calculation is performed in three dimensions with a cubical integration window.

The segmentation was performed by constructing a statistical model for the g and β distributions in the form of a mixture of bivariate Gaussian distributions. In order to construct the model, small regions of interest (ROI) were selected in the image, which contained a single component of the material. The feature variables g and β were calculated inside the selected ROI on a regular grid, with the density of the grid chosen so that the total number of points was sufficiently large (>1000). Fig. 3 shows the ROIs, selected in sample #1 and the distribution of the obtained data points in $\{g, \beta\}$ feature space. The obtained points in i-th ROI were fitted with a bivariate Gaussian distribution

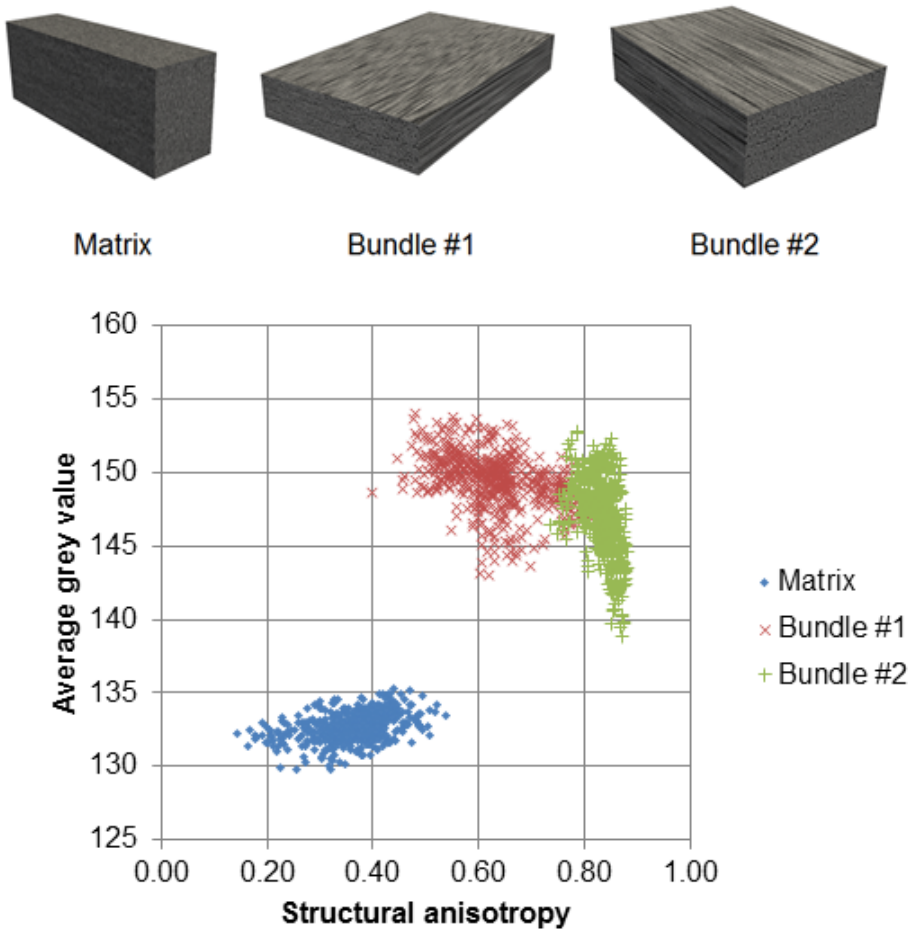

Fig. 3. The selected regions of interest (ROI) from the image of sample #1 (top) and the distribution of the feature variables (bottom) corresponding to the ROIs (both variables have dimensionless units; only the first 500 data points are shown). Bundles #1 and #2 are the regions inside the orthogonal fibre bundles in the material.

$N_i(\boldsymbol{\mu}_i, \boldsymbol{\Sigma}_i)$, where $\boldsymbol{\mu}$ and $\boldsymbol{\Sigma}$ are the mean vector and the covariance matrix of the distribution. Parameters of the distributions were calculated using maximum-likelihood estimation:

$$\boldsymbol{\mu} = \frac{1}{N}\sum \boldsymbol{X}$$

$$\boldsymbol{\Sigma} = \frac{1}{N-1}\sum (\boldsymbol{X} - \boldsymbol{\mu})(\boldsymbol{X} - \boldsymbol{\mu})^T$$

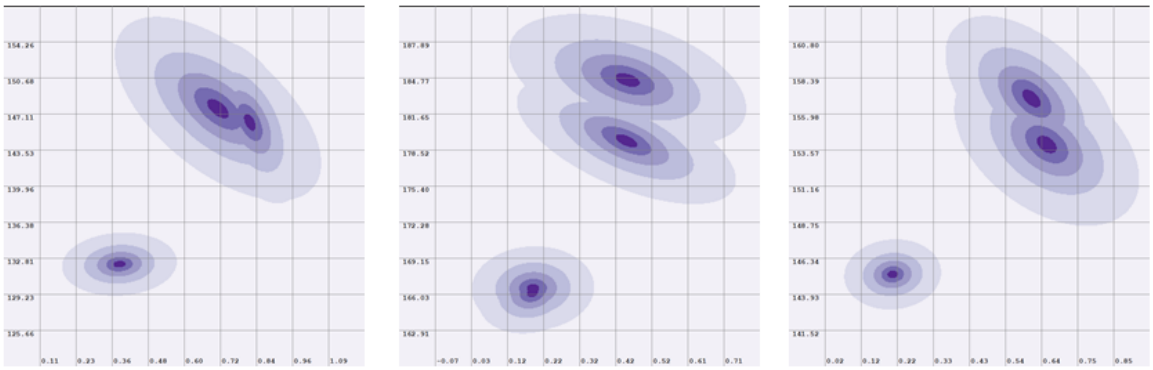

Fig. 4. Probability density distributions in the Gaussian mixture models for the three samples (a – sample #1, b – sample #2, c – sample #3). The rendered density is the maximum value between the components of the mixture. Horizontal axis indicates structural anisotropy, vertical axis – average grey value.

where $\boldsymbol{X} = [g, \beta]^T$. Note that the mean $\boldsymbol{\mu}$ is defined on the basis of the variable g, which is obtained as an average o ver integration window, whereas the $\boldsymbol{\mu}$ itself is an average over a selected ROI. In general, orthogonal yarn systems in micro-CT images have slightly different distributions of feature variables (evidence for this was found in regard to the structural anisotropy [26]). Due to this possible difference, two separate Gaussian distributions were created for the yarns with orthogonal primary orientations. The Gaussian mixture model therefore contained three components: matrix (fluid phase), and two components for the fibre bundles (solid phase). Fig. 4 shows probability density distribution in the Gaussian mixture models of the three samples. Segmentation of the image was done by computing for each spatial point in the image the probabilities P_i for this point to belong to each of the material components:

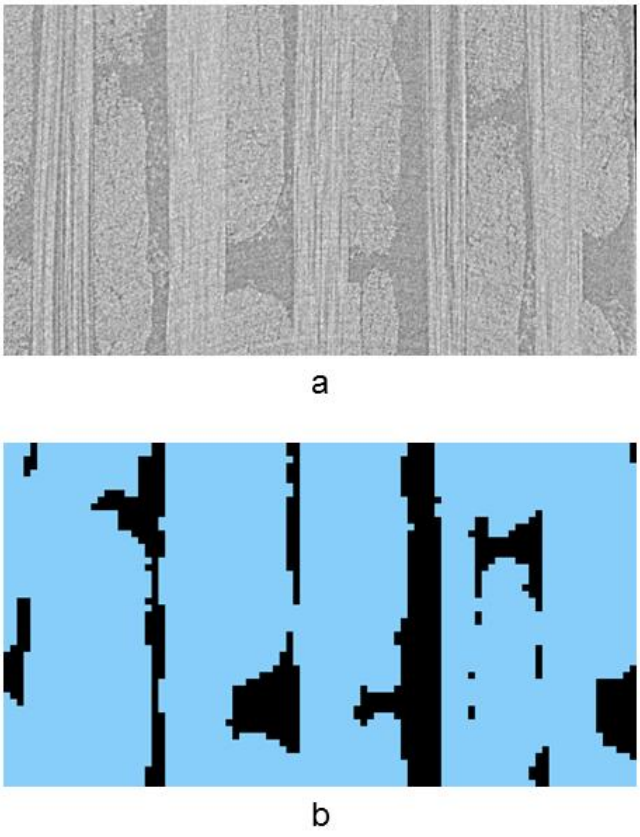

Fig. 5. Comparison of the micro-CT image of a unit cell in sample #2 with the result of segmentation. Blue – solid phase, black – liquid phase.

$$P_i(X) = \frac{1}{\sqrt{(2\pi)^3 |\boldsymbol{\Sigma}_i|}} exp\left[-\frac{1}{2}(\boldsymbol{X} - \boldsymbol{\mu}_i)^T \boldsymbol{\Sigma}_i^{-1} (\boldsymbol{X} - \boldsymbol{\mu}_i)\right]$$

The decision on how to classify each point was made on the basis of maximum probability:

$$C(\boldsymbol{X}) = \underset{i}{\operatorname{argmax}}\, P_i(\boldsymbol{X})$$

Here $C(\boldsymbol{X})$ denotes the classification function, which maps the feature variable values **X** into a finite set of material components, i.e. $C(\boldsymbol{X}) \rightarrow \{matrix, bundle1, bundle2\}$. An example of segmentation and its comparison with the original image, in a unit cell from sample #2, is shown in Fig. 5.

3.1. Statistical model assessment

The Gaussian mixture models created for the purpose of segmentation must contain statistical distributions that are well separated from each other, where the reliable classification decision is required. In the studied case a sufficient distance is required between matrix component and the components of the bundles. Separation between the two types of bundles is not required as they both represent the same phase of the model (solid phase). In addition, it may be useful to check the stability of the distribution parameters to the choice of ROI. In order to make this evaluation, the measure of the distance between Gaussian distributions $N_1(\boldsymbol{\mu}_1, \boldsymbol{\Sigma}_1)$ and $N_2(\boldsymbol{\mu}_2, \boldsymbol{\Sigma}_2)$ known as *Bhattacharya distance* was used, which is defined as follows:

$$D = \frac{1}{8}(\boldsymbol{\mu}_1 - \boldsymbol{\mu}_2)^T \boldsymbol{\Sigma}^{-1}(\boldsymbol{\mu}_1 - \boldsymbol{\mu}_2) + \frac{1}{2}\ln\left(\frac{|\boldsymbol{\Sigma}|}{\sqrt{|\boldsymbol{\Sigma}_1||\boldsymbol{\Sigma}_2|}}\right)$$

where

$$\boldsymbol{\Sigma} = \frac{\boldsymbol{\Sigma}_1 + \boldsymbol{\Sigma}_2}{2}$$

Table 2 shows the calculated Bhattacharya distances between the Gaussian components in the statistical model for sample #2. For the purpose of checking stability to the choice of ROI, an additional matrix ROI was selected in the image. The obtained values show that the distances between matrix and both bundle components are large enough (22.3…32.5). At the same time the distance between the two distributions for the matrix is very small (0.026), which indicates a good stability of the distribution parameters to the choice of ROI.

Table 2. Bhattacharya distance matrix between Gaussian components of the statistical model for sample #2.

	MATRIX #1	**MATRIX #2**	**BUNDLE #1**	**BUNDLE #2**
MATRIX #1	0.000	0.026	23.472	32.500
MATRIX #2	0.026	0.000	22.277	31.189
BUNDLE #1	23.472	22.277	0.000	1.965
BUNDLE #2	32.500	31.189	1.965	0.000

4. Computation of permeability

The result of the image segmentation into solid and fluid domains is used to create the voxel model of a unit cell. The voxel model for computation of fluid dynamics consists of a rectilinear grid with assigned phase indices in each cell of the grid. Voxel models of four unit cells in sample #2 are shown in Fig. 6. Permeability calculations were performed with FlowTex software [14, 27, 28], developed at KU Leuven in collaboration with the Institute for Numerical Simulation at the University of Bonn. FlowTex calculations were successfully benchmarked against finite element CFD ANSYS calculations [29]. The FlowTex software implements the numerical solution of the Stokes equations on a 3D regular grid. The periodic boundary conditions were set along X and Y coordinates (in-plane directions) with wall BC along Z (through-thickness direction). This simulates flow of the resin in the preform during the infusion, where the fluid can propagate in the plane of the preform, bounded by the mould.

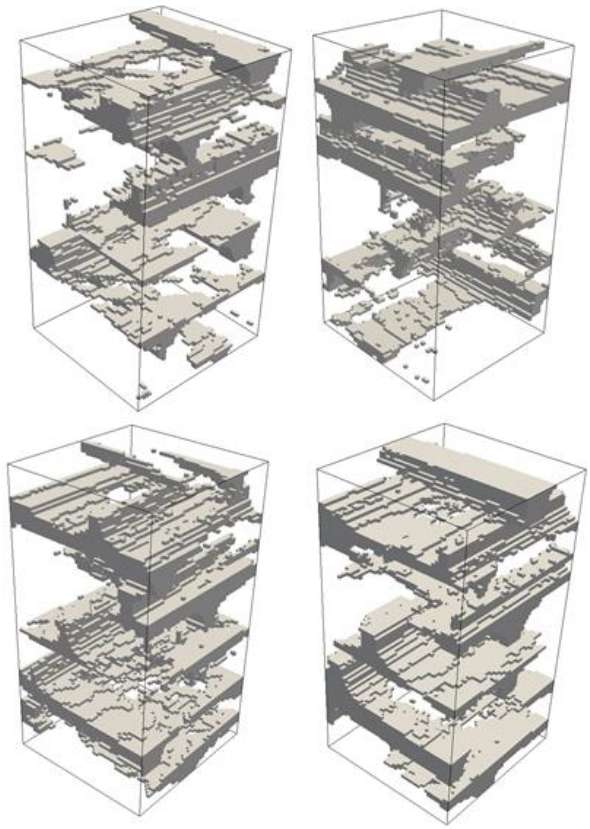

Fig. 6. Flow channels (fluid cells) in the voxel models of four of the unit cells in sample #2. Solid phase voxels are not shown.

5. Results

Fig. 7 shows the calculated permeability for all unit cells in the three studied samples. The permeability varies quite significantly across unit cells, in the range of $(0.5…3.5)\times10^{-4}$ mm^2, which is however in a good agreement with the experimental data $(1.0…2.0\times10^{-4}$ $mm^2)$. Fig. 8 shows average values over the unit cells in the samples. Analysis of the correlation of permeability with the solid volume fraction in the unit cell models showed a significant negative correlation (Fig. 9), i.e. permeability is lower with a higher solid volume fraction. Table 3 provides a summary of the result on permeability calculations and correlation with the solid volume fraction in the models.

Table 3. Average permeability and correlation with solid volume fraction.

	Permeability Ky, mm^2		Permeability Kx, mm^2		Pearson's correlation with solid volume fraction	
	Mean	**STD**	**Mean**	**STD**	**Ky**	**Kx**
Sample #1	7.23E-05	-	1.43E-04	-	-	-
Sample #2	1.26E-04	4.60E-05	2.08E-04	8.23E-05	-0.70	-0.93
Sample #3	1.11E-04	2.72E-05	7.06E-05	3.90E-05	-0.39	-0.89

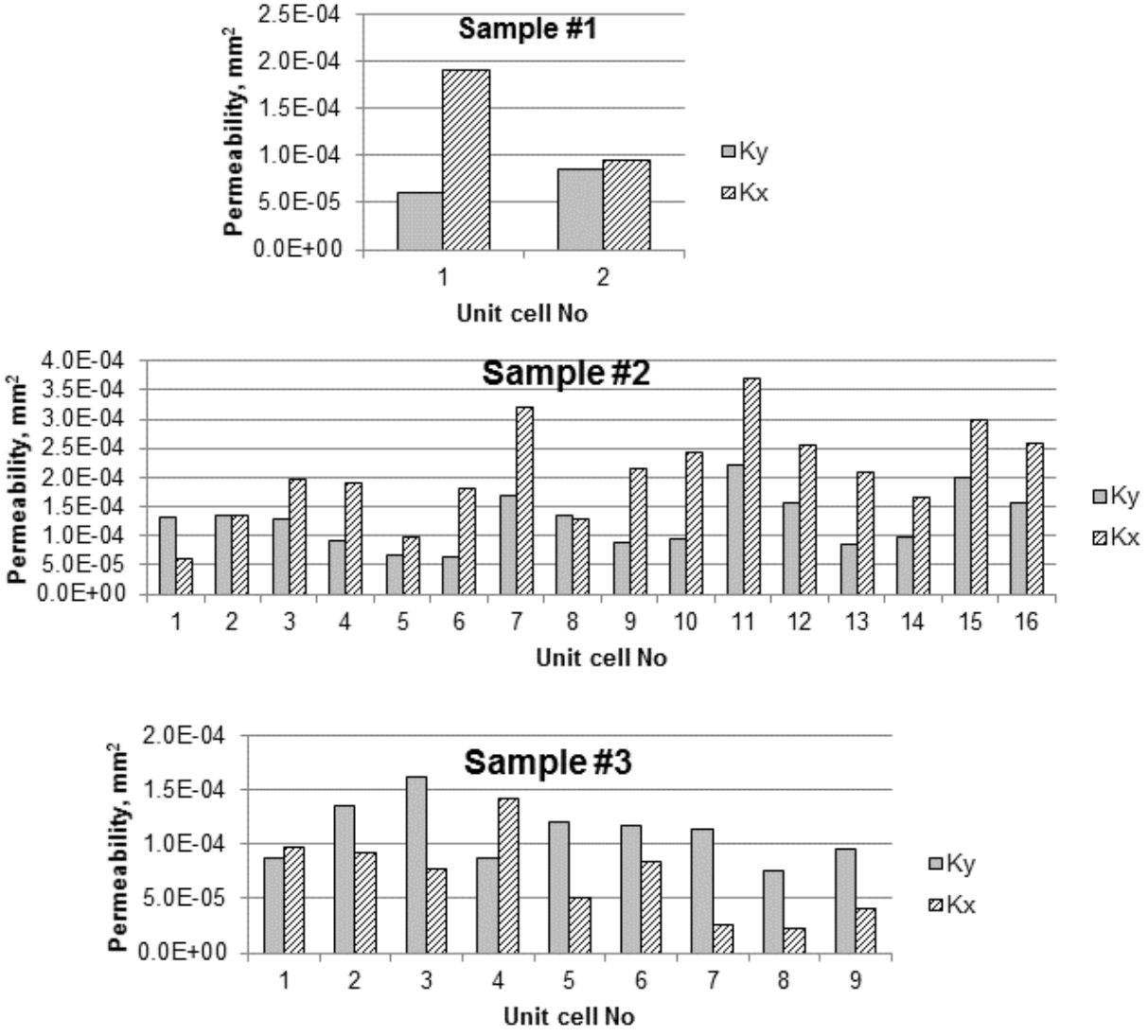

Fig. 7. Permeability of the unit cells in the studied samples.

6. Discussion

The computation of the permeability using voxel models depends on a correct definition of the phases in the model, which is the result of the segmentation procedure. The presented segmentation method is based on the two quantities – average grey value and structural anisotropy – which reflect local physical properties of the material. The average grey value reflects X-ray attenuation of the material, which is proportional to its density and atomic weight (averaged). The structural anisotropy reflects local structural properties of the material and allows making a distinction between matrix, which is structurally isotropic, and reinforcement, which is structurally anisotropic due to the presence of fibers with a particular primary orientation. The construction of a Gaussian mixture model on the basis of the selected subset of data is known as supervised classification. In the case of micro-CT images of composite materials, application of statistical methods is necessitated by the noise, always present in the CT image, and the variability of the material's microstructure, which make all the derived quantities inherently non-deterministic. Compared to the existing approaches for the modelling of composite reinforcements on the basis of experimental data, the presented method does not require any significant manual effort for the data extraction to create a geometrical model. The amount of efforts needed is constant for each dataset, and not proportional to the size of the dataset.

Three samples of the non-crimp carbon epoxy composite were modelled, with the total number of unit cells modelled being 27. Th e results showed a good agreement with the experimental data. The variability of the permeability across unit cells is quite significant, in the range of $(0.5…3.5)\times10^{-4}$ mm^2. The observed difference in the standard deviation of the predicted permeability between samples #2 and #3 might be a result of a different number of unit cells in these samples. In the presence of spatial auto-correlation in the geometry of the preform (such as yarn trajectory [30]), a larger volume of the material will result in a larger dispersion of the predicted properties. This corresponds to the observed difference, as a larger sample #2 shows a higher standard deviation of permeability compared to a smaller sample #3. The computed permeability shows a significant correlation with the solid volume

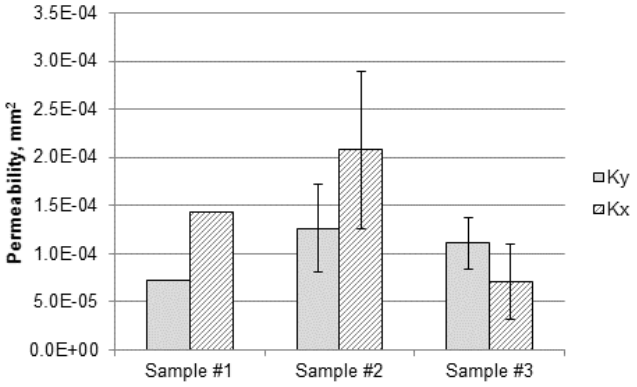

Fig. 8. Average permeability of the samples. Error bars indicate one standard deviation over the unit cells. The error bars at sample #1 are absent because sample #1 contains only 2 unit cells.

fraction in a unit cell. The good agreement of the modelling results with the experimental data indicates that the segmentation procedure provides the phase domain boundaries that are close to the true ones.

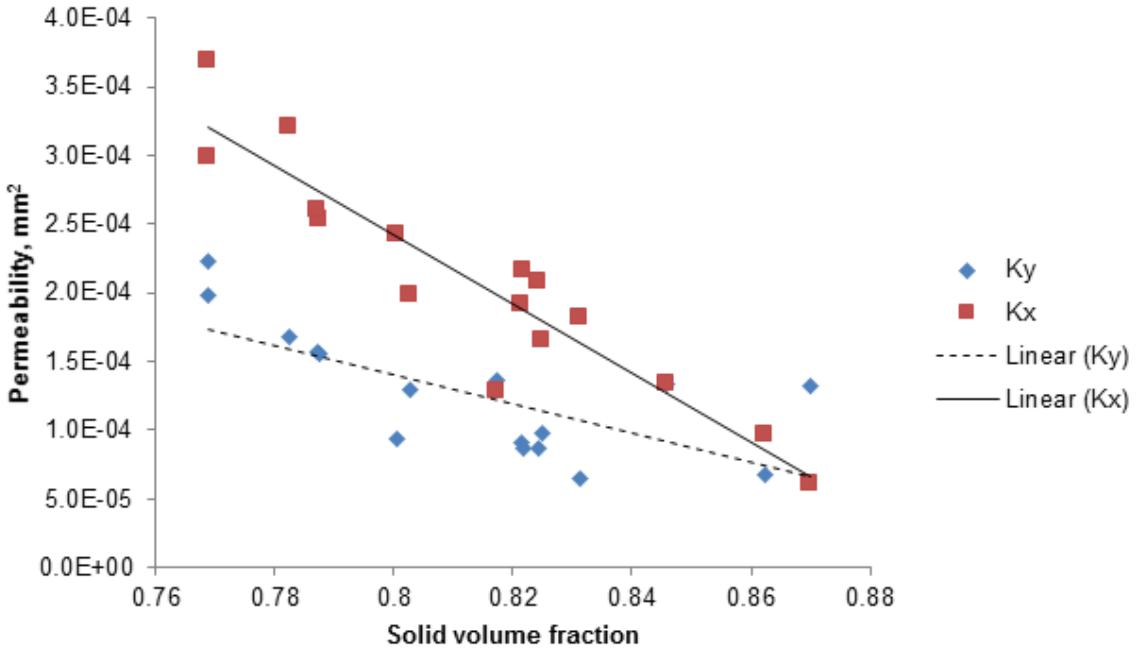

Fig. 9. Distribution of permeability values in unit cells of sample #2 as a function of the solid volume fraction in the unit cell model.

7. Conclusion

We have demonstrated the possibility of correct (within the experimental scatter) calculation of a textile reinforcement permeability based on X-ray micro-computed tomography registration of the textile internal architecture. The image segmentation procedures, used in the paper, provide accurate representation of internal geometry of the textile reinforcement based on images acquired with X-ray micro-computed tomography.

Acknowledgements

This project has received funding from the European Union's Seventh Framework Programme for research, technological development and demonstration under grant agreement no ACP2-GA-2012-314562-QUICOM. XCT measurements were financed by the K-Project ZPT+ supported by COMET programme of FFG and by the federal government of Upper Austria and Styria. The work also benefited from expertise of XCT

Lab in KU Leuven, financed by the Hercules Foundation (project AKUL 09/001: Micro- and nano-CT for the hierarchical analysis of materials).

References

[1] Pillai KM. Modeling the unsaturated flow in liquid composite molding processes: A review and some thoughts. Journal of Composite Materials. 2004;38(23):2097-2118.
[2] Gebart BR. Permeability of Unidirectional Reinforcements for Rtm. Journal of Composite Materials. 1992;26(8):1100-1133.
[3] Cai Z, Berdichevsky AL. An Improved Self-Consistent Method for Estimating the Permeability of a Fiber Assembly. Polymer Composites. 1993;14(4):314-323.
[4] Nordlund M, Lundstrom TS. Effect of multi-scale porosity in local permeability modelling of non-crimp fabrics. Transport in Porous Media. 2008;73(1):109-124.
[5] Rieber G, Jiang JH, Deter C, Chen NL, Mitschang P. Influence of textile parameters on the in-plane Permeability. Composites Part a-Applied Science and Manufacturing. 2013;52:89-98.
[6] Endruweit A, McGregor P, Long AC, Johnson MS. Influence of the fabric architecture on the variations in experimentally determined in-plane permeability values. Composites Science and Technology. 2006;66(11-12):1778-1792.
[7] Nordlund M, Penha DJL, Stolz S, Kuczaj A, Winkelmann C, Geurts BJ. A new analytical model for the permeability of anisotropic structured porous media. International Journal of Engineering Science. 2013;68:38-60.
[8] Endruweit A, Long AC. Analysis of Compressibility and Permeability of Selected 3D Woven Reinforcements. Journal of Composite Materials. 2010;44(24):2833-2862.
[9] Endruweit A, Long AC. A model for the in-plane permeability of triaxially braided reinforcements. Composites Part a-Applied Science and Manufacturing. 2011;42(2):165-172.
[10] Zeng XS, Brown LP, Endruweit A, Matveev M, Long AC. Geometrical modelling of 3D woven reinforcements for polymer composites: Prediction of fabric permeability and composite mechanical properties. Composites Part a-Applied Science and Manufacturing. 2014;56:150-160.
[11] Lekakou C, Edwards S, Bell G, Amico SC. Computer modelling for the prediction of the in-plane permeability of non-crimp stitch bonded fabrics. Composites Part a-Applied Science and Manufacturing. 2006;37(6):820-825.
[12] Lundstrom TS. The permeability of non-crimp stitched fabrics. Composites Part a-Applied Science and Manufacturing. 2000;31(12):1345-1353.
[13] Takano N, Zako M, Okazaki T, Terada K. Microstructure-based evaluation of the influence of woven architecture on permeability by asymptotic homogenization theory. Composites Science and Technology. 2002;62(10-11):1347-1356.
[14] Verleye B, Croce R, Griebel M, Klitz M, Lomov SV, Morren G, et al. Permeability of textile reinforcements: Simulation, influence of shear and validation. Composites Science and Technology. 2008;68(13):2804-2810.
[15] Nordlund M, Lundstrom TS, V F, Jakovics A. Permeability network model for non-crimp fabrics. Composites Part a-Applied Science and Manufacturing. 2006;37(6):826-835.
[16] Endruweit A, Long AC, Robitaille F, Rudd CD. Influence of stochastic fibre angle variations on the permeability of bi-directional textile fabrics. Composites Part a-Applied Science and Manufacturing. 2006;37(1):122-132.
[17] Endruweit A, Long AC. Influence of stochastic variations in the fibre spacing on the permeability of bi-directional textile fabrics. Composites Part a-Applied Science and Manufacturing. 2006;37(5):679-694.

[18] Lundstrom TS. A statistical approach to permeability of clustered fibre reinforcements. Journal of Composite Materials. 2004;38(13):1137-1149.
[19] Vanaerschot A, Cox BN, Lomov SV, Vandepitte D. Stochastic framework for quantifying the geometrical variability of laminated textile composites using micro-computed tomography. Composites Part a-Applied Science and Manufacturing. 2013;44:122-131.
[20] Vanaerschot A, Cox BN, Lomov SV, Vandepitte D. Stochastic multi-scale modelling of textile composites based on internal geometry variability. Computers & Structures. 2013;122:55-64.
[21] Blacklock M, Bale H, Begley M, Cox B. Generating virtual textile composite specimens using statistical data from micro-computed tomography: 1D tow representations for the Binary Model. Journal of the Mechanics and Physics of Solids. 2012;60(3):451-470.
[22] Delerue JF, Lomov SV, Parnas RS, Verpoest I, Wevers M. Pore network modeling of permeability for textile reinforcements. Polymer Composites. 2003;24(3):344-357.
[23] Schell JSU, Renggli M, van Lenthe GH, Muller R, Ermanni P. Micro-computed tomography determination of glass fibre reinforced polymer meso-structure. Composites Science and Technology. 2006;66(13):2016-2022.
[24] Hahn C, Binetruy C, Hinterhoelzl R. A Simulation-Based Method of Permeability Prediction for RTM Process Simulation. In: Hoa SV, Hubert P, editors. International Conference on Composite Materials 2013 (ICCM-19), vol. 9 Montreal, Quebec, Canada2013. p. 6122-6133.
[25] Loendersloot R. Permeability of non-crimp fabric preforms. In: Lomov SV, editor. Non-crimp fabric composites: manufacturing, properties and applications: Woodhead Publishing; 2011. p. 166-215.
[26] Straumit I, Wevers M, Lomov SV. Influence of the orientation of fibrous structures in a composite material relative to the sample's rotation axis on the local apparent degree of anisotropy derived from micro-CT. Bruker Micro-CT User Meeting, Oostende, Belgium2014. p. 25-29.
[27] Verleye B, Lomov SV, Long A, Verpoest I, Roose D. Permeability prediction for the meso-macro coupling in the simulation of the impregnation stage of Resin Transfer Moulding. Composites Part a-Applied Science and Manufacturing. 2010;41(1):29-35.
[28] Verleye B, Morren G, Lomov SV, Sol H, Roose D. Userfriendly permeability predicting software for technical textiles. 5th Industrial Simulation Conference 2007. 2007:455-458.
[29] Swery EE, Meier R, Lomov SV, Hahn C, Kelly P, Straumit I. Verification of FlowTex solver using Ansys CFX - Examining the permeability prediction method on a range of textile architecture models. 16th European Conference on Composite Materials (ECCM-16), Seville, Spain2014.
[30] Vanaerschot A., Cox B. N., Lomov S. V., Vandepitte D. Simulation of the cross-correlated positions of in-plane tow centroids in textile composites based on experimental data. Composite Structures. 2014;116:75-83.

List of figures: